crystals

MDPI

Review

GaAs Nanowires Grown by Catalyst Epitaxy for High Performance Photovoltaics

Ying Wang [1,2], Xinyuan Zhou [2], Zaixing Yang [3], Fengyun Wang [4], Ning Han [1,2,*], Yunfa Chen [1,2,*] and Johnny C. Ho [5,*]

1 State Key Laboratory of Multiphase Complex Systems, Institute of Process Engineering, Chinese Academy of Sciences, Beijing 100190, China; wangying@ipe.ac.cn
2 Center for Excellence in Regional Atmospheric Environment, Institute of Urban Environment, Chinese Academy of Sciences, Xiamen 361021, China; zhouxinyuan14@mails.ucas.ac.cn
3 Center of Nanoelectronics and School of Microelectronics, Shandong University, Jinan 250100, China; zaixyang@sdu.edu.cn
4 College of Physics and Cultivation Base for State Key Laboratory, Qingdao University, Qingdao 266071, China; fywang@qdu.edu.cn
5 Department of Materials Science and Engineering, City University of Hong Kong, Kowloon, Hong Kong, China
* Correspondence: nhan@ipe.ac.cn (N.H.); chenyf@ipe.ac.cn (Y.C.); johnnyho@cityu.edu.hk (J.C.H.); Tel.: +86-010-6255-8356 (N.H.)

Received: 13 August 2018; Accepted: 27 August 2018; Published: 29 August 2018

Abstract: Photovoltaics (PVs) based on nanostructured III/V semiconductors can potentially reduce the material usage and increase the light-to-electricity conversion efficiency, which are anticipated to make a significant impact on the next-generation solar cells. In particular, GaAs nanowire (NW) is one of the most promising III/V nanomaterials for PVs due to its ideal bandgap and excellent light absorption efficiency. In order to achieve large-scale practical PV applications, further controllability in the NW growth and device fabrication is still needed for the efficiency improvement. This article reviews the recent development in GaAs NW-based PVs with an emphasis on cost-effectively synthesis of GaAs NWs, device design and corresponding performance measurement. We first discuss the available manipulated growth methods of GaAs NWs, such as the catalytic vapor-liquid-solid (VLS) and vapor-solid-solid (VSS) epitaxial growth, followed by the catalyst-controlled engineering process, and typical crystal structure and orientation of resulted NWs. The structure-property relationships are also discussed for achieving the optimal PV performance. At the same time, important device issues are as well summarized, including the light absorption, tunnel junctions and contact configuration. Towards the end, we survey the reported performance data and make some remarks on the challenges for current nanostructured PVs. These results not only lay the ground to considerably achieve the higher efficiencies in GaAs NW-based PVs but also open up great opportunities for the future low-cost smart solar energy harvesting devices.

Keywords: GaAs nanowires; catalyst epitaxy; photovoltaics; optical absorption; Schottky barrier

1. Introduction

Energy crisis has always been a world-wide concern, as natural fossil fuel sources are becoming increasingly less available and more expensive [1–4]. Besides, air pollution from consumption of fossil fuels is severely threatening the living environment of human beings [5,6]. Thus, there is an urgent demand for developing alternative renewable clean energy sources. Among various energy sources including hydroelectricity, wind, and geothermal energy, sunlight is one of the most prospective candidates for its abundance and zero-emissions [7–9]. It is estimated that the energy from sunlight

striking the earth in one hour can meet our annual global energy consumption. However, the solar PVs converting sunlight into electricity only constitutes a small fraction (<1%) of the global energy supply [10,11]. The main factors limiting the widespread adoption of PV are its low power conversion efficiency (PCE) and high cost. These challenges are hard to overcome but the potential benefits are worth the efforts.

In the past decades, significant researches have focused on increasing the PCE of PV while simultaneously reducing the production cost [12–16]. Generally, the cost of commercial and domestic PVs to consumers is related to the system energy cost (in $/kWh), which includes the module cost (depends on the PCE) and the balance of system cost (equals the module cost) [12]. As shown in Figure 1, higher module cost can be tolerated if the module PCE increases. For the first generation technology (majority of today's PV market), PV devices are defined as p-n junctions formed in single crystal or multi-crystalline Si substrates (cost ~0.3 $/kWh) [17,18]. Second generation PV reduces the material usage by depositing various thin films on inexpensive metal foil or glass substrates, such as amorphous Si film [19,20], copper indium gallium diselenide (CIGS) [21,22], and III/V semiconductor film [23,24]. Although recorded overall cost (~0.1 $/kWh) is achieved by current-day PV technology, the limitation of low material quality and poor PCE make it difficult to compete with that of conventional energy sources. Therefore, third-generation device concepts mainly aim to overcome the Shockley-Queisser efficiency limit for a single p-n junction (~33%, 1 Sun), while reducing production cost [25–32]. As one strategy, multijunction solar cells based on thin films of III/V compound semiconductor materials commonly employ a stack of p-n junctions and their PCE can infinitely approach the theoretical 68% at 1-sun intensity (thermodynamic limit) [13,33–35]. For example, a measured 1-sun PCE of 34.1% has been achieved in a triple-junction solar cell. Under concentrated sunlight (302 sun), the record PCE for any PV cell is 44.4% [36]. However, the very expensive materials, fabrication, and focusing optics for III/V multijunction cells limit their large-scale fabrication. Currently, a second strategy to promote PCE of PVs is to develop cost-effective candidates with high PV performance, such as polymer solar cells (PSCs) and perovskite solar cells (PVSCs). In particular, perovskite solar cells have the combination of some key attributes including large absorption coefficients (10^5 cm^{-1}), high charge carrier mobilities (10^1 cm^2 V^{-1} s^{-1}), the tunability of optical properties and various deposition protocols, which enables perovskite solar cells to reach a certified efficiency of 22.7% [37,38]. However, many challenges remain to be solved before polymer and perovskite solar cells can be considered for real-life applications, including incorporating novel light harvesting materials, optimizing device architectures, developing conductive materials for the transparent electrodes, and especially improving the long-term stability of PVs. The other emerged strategy of circumventing assumptions of the Shockley-Queisser is PV designs utilizing nanostructured materials, such as nanocrystals (based on multiple exciton generation (MEG) with limiting efficiency of ~44%) [39–42], nanotubes [43–45], nanopillars [46–48], and NWs [49–58]. With the advantages of significant reduction in material usage, strong light absorption and efficient charge separation, nanostructured solar cells hold great promise for reaching the demand of 0.03–0.05 $/kWh by third-generation technologies.

Among all the nanostructured solar cells, one-dimensional (1D) NW-based cells have been widely adopted due to their versatility, stability, the reduced minority-carrier lifetime, and optical reflectivity, in addition to their compatibility with current Si-based microelectronics [31,59–70]. With high PCE and extraordinary radiation hardness, GaAs NW is one of the most important nanostructures and has been long concerned. For direct-bandgap GaAs NWs, optical interference and guiding effects promote the light absorption by two–10 times [71–74]. For example, Krogstrup et al. reported a measured solar conversion efficiency of 40% utilizing the light-concentrating property of a single standing GaAs NW [74]. Furthermore, heterostructured junctions and passivation have been intensely investigated for efficiently carrier separation and collection [75–78]. Nowadays, design of transparent or wearable NW device also paves the way of PV applications by making it more intelligent [79–81]. The synthesis of 1D GaAs NW by self-catalyzed or self-assisted method has recently been provided in [82–85], with the

goal of growing gold-free GaAs NWs. For example, Dong et al. reported the first gallium-catalyzed hydride vapor phase epitaxy (HVPE) growth of long (>10 μm) GaAs NWs on Si(111) substrates with an ultrahigh growth rate (>1 μm/min) and pure zincblende crystal structure [86]. Unlike metal organic vapor phase epitaxy (MOVPE), this reported HVPE method makes use of metal chlorides for group III source, which will benefit for reducing the material cost. More detailed descriptions on self-catalyzed III/V NWs can be found in the literatures [83,85,87–89]. In this review, we focus on recent works on the catalyst epitaxial growth of GaAs NWs and their PV performance. Towards high-quality NW materials and high PCE for PV, the structure-property relationships of NWs will be highlighted in this review. After that, we conclude the manipulated methods of NW growth on amorphous substrates and important device issues including optical absorption, tunnel junctions, and contact configuration.

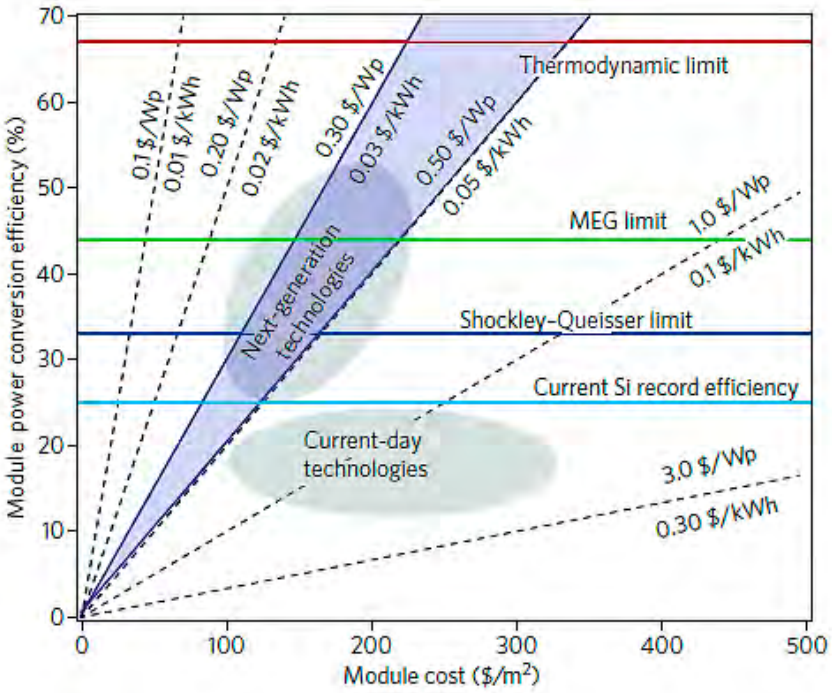

Figure 1. Relationship between power conversion efficiency, module areal costs, and cost per peak watt (in $/Wp). The light blue line represents the current laboratory record efficiency for bulk crystal silicon while the blue horizontal line is the Shockley-Queisser limit for single-junction devices. Third-generation device concepts increase the limiting efficiency (the limit for multiple exciton generation (MEG) is indicated as the green line). The thermodynamic limit at 1 sun is shown as the red line at 67% and can be reached by an infinite stack of p-n junctions. For next-generation technologies the goal is to reach 0.03–0.05 $/kWh, denoted by the blue shaded region. Adapted with permission from [12].

2. GaAs NW Growth via Catalyst Epitaxy

Most NWs are synthesized epitaxially on a single crystalline GaAs wafer via VLS or VSS growth mechanisms by molecular beam epitaxy (MBE) or chemical vapor deposition (CVD) techniques [90–92]. Apart from the absence of expensive epitaxial substrates, catalyst epitaxy by metal nanoparticles (NP, such as Au, Ni, Ag, and Pd for GaAs NW) has been verified a cost-effective and versatile manipulating strategy for synthesizing NWs on amorphous SiO_2 or glass substrates [93,94]. The catalyst seeds act as one of the most important parameters in directing the growth of NWs. Emphasizing the solid source CVD technique, we go over the growth mechanisms, typical manipulations of GaAs NWs growth, and their crystal structures.

Notably, there are other techniques for NW growth except the conventional VLS and VSS method, such as the well-known laser ablation method reported by the Lieber group and the newly invented Aerotaxy technique [95–97]. In particular, the Aerotaxy method can provide low-cost axial GaAs

pn-junctions by a continuous, high-throughput and substrate-less process. Together with our technique of catalyst epitaxy, these new technologies to synthesize NWs pave the way for industrial production of NW-based PVs.

2.1. The VLS and VSS Growth Methods

Figure 2 depicts the typical schematic illustration of the CVD growth setup of a two-zone tube furnace [98]. The solid source is evaporated at the center of the upstream zone and transported by a carrier gas of hydrogen to the downstream zone. The growth substrate with pre-coated NP catalysts is placed in the middle of the downstream zone with a distance of 20 cm away from the source. Then the source and substrate are subject to different temperatures, evaporating the precursors for growth of NWs. If the substrate is firstly annealed at higher temperature and then cooled down to the growth temperature of NWs, it is called two-step growth method, which is adopted for tuning of the catalyst composition and the subsequent epitaxial growth of NWs.

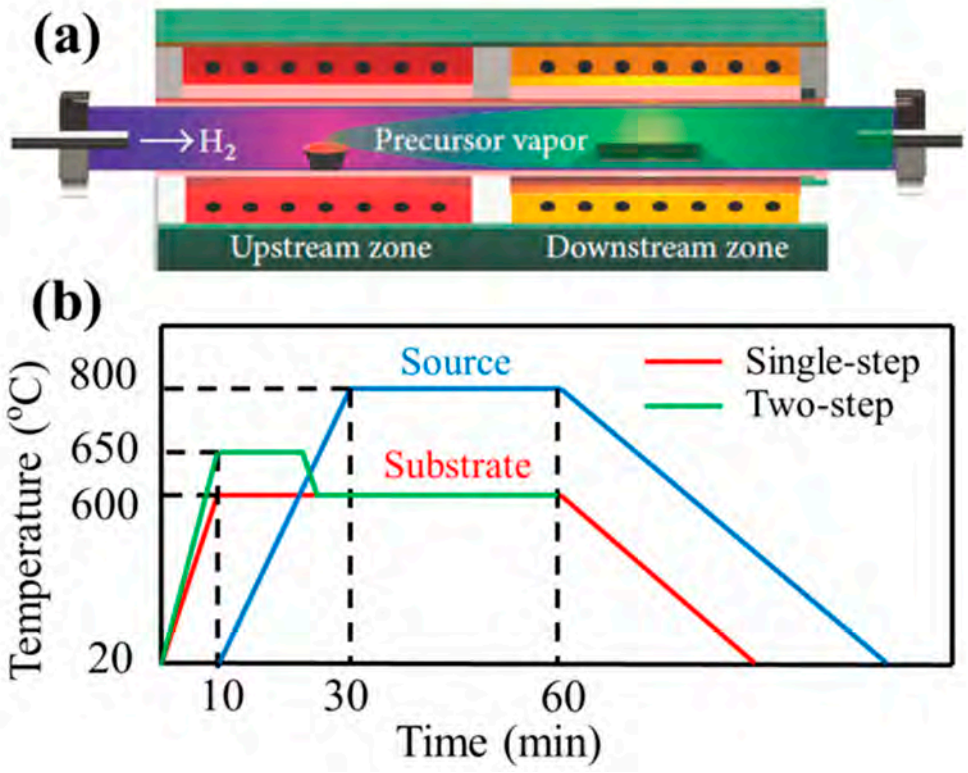

Figure 2. (**a**) Schematic illustration of the catalytic chemical vapor deposition (CVD) growth of GaAs nanowires (NWs) and (**b**) the temperature profiles. The typical dual-zone horizontal tube furnace, one zone is used for the solid source (upstream) and the other for the sample (downstream). Adapted with permission from [98].

The differences in the growth behavior of GaAs NWs are largely determined by the interaction between the source material and the catalytic NP. The key feature of the VLS growth mechanism is the liquid state of the metal alloy tip during the NW growth, which occurs by the formation of a eutectic melt. Once the alloy tip forms a eutectic, the excess material that is adsorbed from the vapor precipitates out in the form of a nanowire. Typically, Au catalyzed growth of GaAs NW has been confirmed as a standard VLS mode. As an example, Zhang et al. reported the non-linear relationship between the Au NP size and the final GaAs NW diameter and attributed it to the different Ga solubilities in varied sizes of Au particles [99]. Unlike the VLS mechanism, in VSS, the metal alloys exit as solid particles. For example, Han et al. found that thin GaAs NWs could be grown epitaxially in the VSS mode from

the Ni-Ga alloy seeds using Ni nanoparticles as the catalyst [100,101]. Recently, there are even several ordered layers found in the interfaces of Au-GaAs by in-situ high-resolution transmission electron microscopy (HRTEM), inferring a quasi-VSS growth mechanism even in the VLS growth mode [102]. Anyway, in both cases, the crystal quality and growth orientation of high performance NWs are found to be systematically controlled by tuning the composition, size, and phase of catalyst seeds.

2.2. GaAs NW Growth via Catalyst Epitaxy

The development of GaAs NW-based PV devices depends on the ability to fabricate NWs with tight control over their properties. The challenge is to produce NWs free of crystallographic defects with uniform diameters and with high purity. During the VLS or VSS growth with CVD technique, the most important aspects in controlling metal-seeded NW growth are linked to the NP seeds together with the growing crystal and its environment (growth temperature, pressure, carrier gas, etc.) [103–108]. In particular, manipulating the metal NP and its alloy composition have a strong impact on the resulting NW, regarding that the growth of NW initiates at the catalyst/NW interface [92,94,109].

Various catalytic NPs including Au, Pd, Ag, and Ni have been adopted for GaAs NW growth. Most of the metallic NPs in previous reports were prepared by thermally pre-depositing a thin film and then annealing it into NPs at a high temperature (for example 800 °C for Au film) [56,92,110]. After detailed investigation on the catalyst/NW interface, the epitaxy relationship is found for most NWs as shown in Figure 3 [100]. Taking Ni/GaAs NW as an example, the Ga atom alignments have the minimal lattice mismatch in the NiGa alloy catalyst and the GaAs NW body, which therefore minimizes the total energy and thus is thermodynamically favorable for high quality NW growth. In this context, the NW structures such as crystal phase, growth orientations can be tuned by the catalyst engineering.

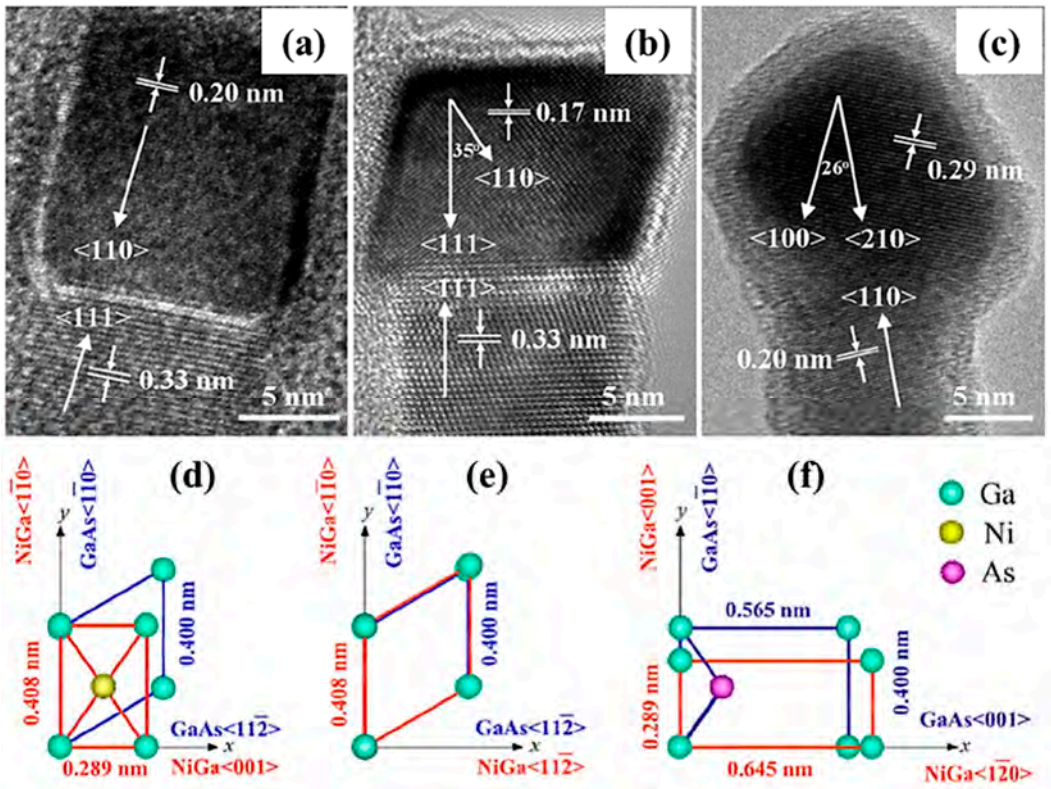

Figure 3. NiGa catalyst and GaAs NW epitaxy relationships. (**a**) NiGa(110) | GaAs(111), (**b**) NiGa(111) | GaAs(111) and (**c**) NiGa(210) | GaAs(110). (**d**–**f**) are the schematics of relationship in (**a**–**c**). Adapted with permission from [100].

2.3. Evaluations of the Catalyst Epitaxy

There are several benefits for the catalyst expitaxy growth of III–V NWs. Firstly, the crystal defects are minimized. GaAs materials have the zinc blende (ZB) crystal structure in bulk form, because the wurtzite (WZ) crystal phase is not thermodynamically stable under ambient conditions [111]. Furthermore, GaAs NWs don't normally have threading dislocations, because they are not stable in GaAs NWs [112,113]. Whereas, the as-grown NWs exhibit ZB, WZ or a mixed crystal phase with stacking defaults or kinking along the growth direction of NW. Sanchez et al. also described stable topologically protected line defects in GaAsP NWs in their latest work, which have not been previously discovered [114]. These defects act as the nonradiative recombination centers, which have great influence on the NW performances. Crystal phase-dependent nanophotonic and electronic properties have been reported by numerous groups [111,115,116]. Hoang et al. found that the WZ structure had a larger bandgap (~29 meV) compared to ZB, which explained the blue-shift of the corresponding light absorption for WZ NWs [115]. Jancu et al. observed the formation of type II heterostructures in WZ GaAs NW with a mixed ZB phase [116]. All these results emphasized the importance of crystal phase-engineering during the NW growth. By introducing beryllium (Be) doping during the NW core growth, pure-ZB GaAs/GaAsP core-shell NWs with high regular morphology were synthesized directly n p-type Si(111) substrates [117]. In our previous study, the catalyst epitaxial grown GaAs NWs are single crystalline with minimized crystal defect as revealed by photoluminescence and Raman spectroscopy, which have a high PCE of ~16% [81]. In the meanwhile, the catalyst epitaxial grown GaSb NWs have a high hole mobility of 300–400 cm^2/Vs, due to the diminished crystal defects by the Au and Pd catalyst epitaxial growth method [118].

Secondly, the NW orientation can be controlled by the selective growth on certain crystal planes of the catalyst with minimal lattice mismatch with the NW body. In the literature, the growth direction of GaAs NWs in MBE is highly dependent on a wide variety of growth conditions, the substrate, the catalytic supersaturation, the droplet wetting and the pre-nucleation conditions [74,90,119]. GaAs(111)B substrates result in <111> NWs that are orthogonal to the substrate surface [120]. While for GaAs(111)A substrates, controllable switching between <111>B and <111>A growth directions is achieved using a simple combination of nucleation and surface energy engineering of the Au seeds [109]. More than 70% of the NWs grown on Si(111) substrates have equivalent <111> directions, but the Si(100) substrates usually result in titled NWs [120]. The case turns more complicated for the catalyst epitaxial on amorphous substrates, such as on glass and SiO_2, in which the NW nucleation is more or less scattered and randomized. In our previous work, various growth orientations such as <111>, <110>, <331>, and <311>GaAs NWs were observed due to the lack of crystalline template to direct the NW growth. With the engineered high Ga supersaturation with smaller Au NPs, NWs can be manipulated to grow unidirectionally along <111> with a higher growth rate and less defect concentration under similar growth condition [94]. A two-temperature method can also be used to optimize the pre-nucleation of catalyst alloy in order to control the crystal quality and orientation for the uniform NW growth [121]. In Pd catalyzed GaSb NWs growth, pure <111> NWs are grown by the Pd_5Ga_4 catalyst epitaxy, which have high hole mobility of 300–400 cm^2/Vs [118].

Third, there would be sharp Schottky barrier between the catalyst and the NW body. There are abundant surface states such as dangle bonds on the surface of GaAs NWs, due to the large surface-to-volume ratio. These surface states would pin the surface Fermi level near the intrinsic position, which makes far lower Schottky barrier of metal-semiconductor Schottky contact than the theoretical one as shown in Figure 4 [58]. For example, thermally deposited Au electrode has only small Schottky barrier of ~0.1 eV as shown in Figure 4d, far lower than the work function difference of Au (5.1 eV) and GaAs (4.6 eV). In contrast, the atomically attached Au catalyst has sharp Schottky barrier of ~0.6 eV as shown in Figure 4b, which would be due to the unpinned surface Fermi level of GaAs by diminishing the surface states in the Au/GaAs interfaces. Similar results are also found for the Ga/GaAs interface, where a sharp Schottky barrier of ~1.0 eV is estimated between the axially heterostructured Ga/GaAs NWs as shown in Figure 4e,f [58]. Therefore, the sharp Schottky barrier

of metal catalyst and the NW body would benefit for the nanodiodes design and fabrication by eliminating the surface Fermi level pinning effect in the nanomaterials.

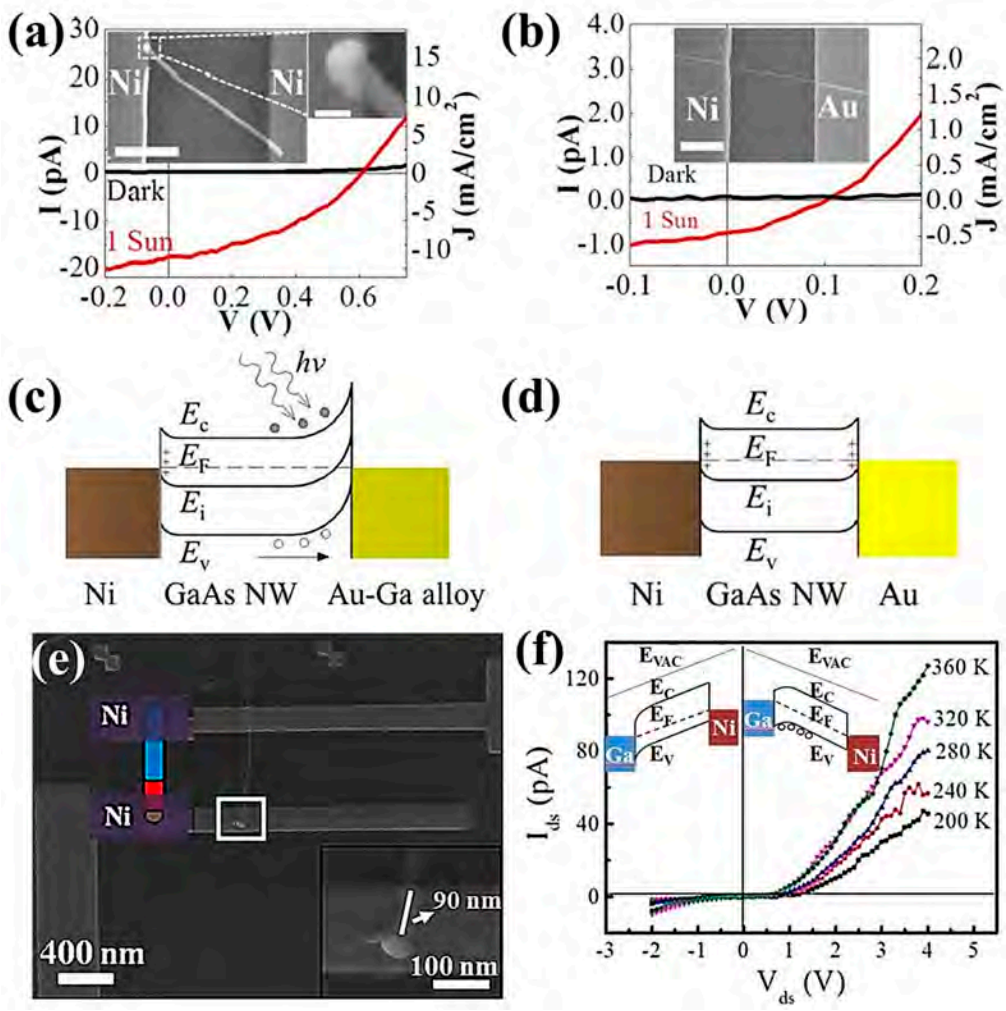

Figure 4. Schottky barriers of the catalyst/NW interface. (**a**,**c**) Typical I–V characteristics, scanning electron microscope (SEM) image and energy band diagram of the single GaAs NW photovoltaic device with Ni and the Au–Ga alloy tip. (**b**,**d**) I–V characteristics, SEM image and energy band diagram of the NW photovoltaic device with deposited Ni and Au. (**e**,**f**) device SEM and I–V curves of the Ga/GaAs interface. Adapted with permission from [58,122].

Apart from these benefits, there are also drawbacks and challenges, which may limit the application of the technique of catalyst expitaxy. The most concerned problem is the contamination of foreign-metals during the growth of NWs, which has been reported to reduce the electron mean free path and degrade their electronic properties [123]. The direct imaging of Au atoms within GaAs NWs demonstrated the Au doping values in the order of 10^{17}–10^{18} cm^3, which makes ballistic transport through the NWs practically inaccessible. Besides, Breuer et al. showed that the internal quantum efficiency of PV device is systematically much lower for the Au-assisted nanowires than that for the Au-free ones [124]. The incorporation of atoms from the Au catalyst droplet also makes the achieved NWs not well suited for integration with silicon electronic platforms [86]. Consequently, there has been considerable effort in developing catalyst-free growth techniques, like self-catalyzed synthetic modes. However, it is still difficult to control the morphology, crystal phase and defects of NWs during the catalyst-free growth. The problem becomes more serious for the growth on amorphous substrates.

Hence, the catalyst-free growth methods do not as yet provide a full alternative to the gold-assisted growth of III/V NWs.

2.4. Catalyst Engineering for Tuned Growth of GaAs NW

First, narrower diameter distributions have always been expected after annealing the Au catalyst films [92,121]. With minimized Ostwald ripening during the air-annealing process, we obtained stabilized Au NPs and corresponding uniform p-type GaAs NWs with diameter distribution of 24% [92]. Second, the catalytic supersaturation has a significant influence over the growth, which is often associated with the Gibbs-Thomson effect [101]. As shown in Figure 5, we have presented a facile approach to control the crystal structure, defects, orientation, growth rate, and density of GaAs NWs by tailoring the Ga supersaturation in the starting Au_xGa_y alloy [94]. High Ga supersaturation (the low-melting-point catalytic alloys including AuGa, Au_2Ga, and Au_7Ga_3 with Ga atomic concentration > 30%) with small Au catalysts (diameter < 40 nm) are preferred to obtain high-quality <111> directional GaAs NWs with the pure zinc blende phase. Third, an additional high-temperature (640–660 °C) nucleation step before the regular growth step has been found helpful for the formation of high Ga supersaturated Au_7Ga_3 and Au_2Ga alloy seeds, which is identified as the two-step growth method [121]. By comparing the morphology, diameter distribution, orientation, photoluminescence and Raman spectroscopy of NWs in Figure 6, improved crystal quality, minimal defect concentration, as well as uniform growth orientation have been achieved utilizing a two-step growth method.

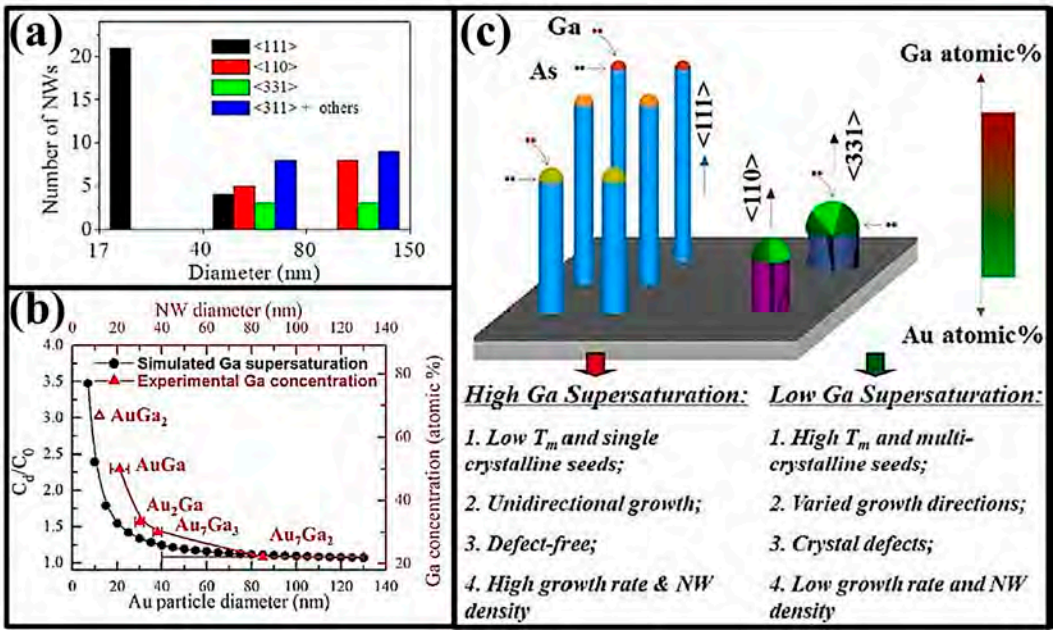

Figure 5. Supersaturation-controlled growth of GaAs NWs. (**a**) Growth direction statistics of grown GaAs NWs. (**b**) Simulation of the Ga supersaturation in Au nanoparticles with various diameters (black line) and the experimental results of catalytic Ga concentration with different NW diameters (red line). (**c**) The schematic illustration of GaAs NW growth rate, density, orientation, and crystal phase change with Ga supersaturation in Au catalyst with different diameters. Adapted with permission from [94].

On the other hand, near-monodisperse, shape-controlled, and core-shell heteostructured synthesis of nanocrystals has been available by wet-chemical methods [125–128]. For this noble-metal system, colloidal nanocrystals possess well-defined surfaces and morphologies, because their nucleation and growth are controlled at the atomic level. In comparison to more conventional spherical particles, the highly faceted, shaped metal NPs are closely related to the initial growth kinetics of III/V NWs

at identical growth conditions. Pin et al. synthesized Au nanocubes with well-defined Au(100) crystalline planes by incorporating a surfactant of hexadecyl trimethyl ammonium bromide (CTAB) in the synthesis, and they found the InAs NWs grown with shape-controlled Au seed particles exhibited an increased absorption of In leading to the observed growth rate enhancement [129]. Surprisingly, compared to the NPs obtained by annealing Au film, colloidal Au NPs with the same spherical shape have entirely different catalytic properties. In our recent work, the single-crystalline heterostructured Ga/GaAs NWs with sharp hetero-Schottky interfaces have been successfully synthesized by utilizing colloidal Au NPs with the diameter of 10 nm, which was never observed in the case of annealed Au NPs [122]. To achieve the practical PV applications of nanocrystal-seeded NWs, future studies are still needed to further clarify the influence of the metal NP size, facet, and composition on the supersaturated alloy seeds and the NW growth speed, crystal phase, and defects.

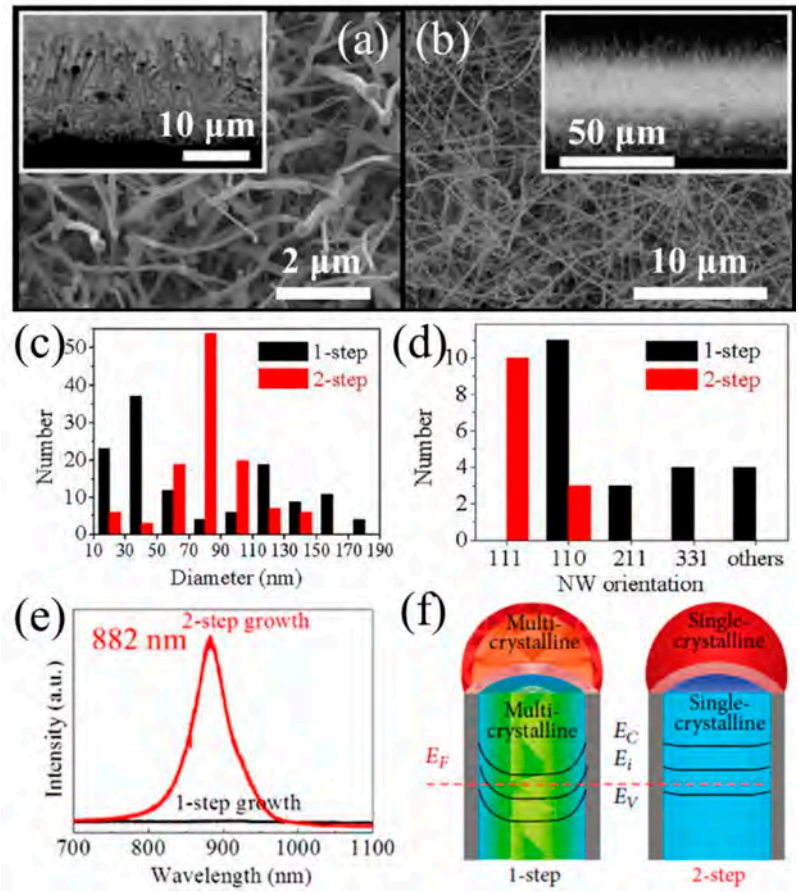

Figure 6. Comparison of the single-step and two-step growth method. (**a**,**b**) SEM images of the single-step and two-step grown NWs. Insets: the corresponding cross-sectional SEM images illustrating the length of the NWs. (**c**,**d**) Diameter distribution and NW growth orientation statistic of GaAs NWs grown by the 12 nm thick Au catalyst. (**e**) Room temperature photoluminescence (PL) spectra, showing a good crystal quality of the two-step grown NWs. (**f**) Cross-sectional view of NWs with the corresponding crystal quality and equilibrium energy band diagram at the zero gate bias. Adapted with permission from [121].

3. The Structure-Property Relationships

Applications of NWs in electronics, photonics, optoelectronics, and PV are strongly influenced by structural parameters including morphology, phase purity, orientation, or lattice strain. In this regard, investigating correlation of structure-property is necessary but challenging. One major problem is that it is merely impracticable to fabricate the same NW into a device for detailed electrical and optical measurements

after the structure evaluation by high-resolution transmission electron microscopy (HRTEM). At the same time, the structural composition of individual wires may be not homogeneous, which adds the difficulty of deciding the structure-property relationships. Recently, significant progress has been made through the nanomanipulation of individual NW and in situ microscopic characterization [130–132]. Fu et al. develop the following experimental method and process to investigate the correlation between the structural (crystal phase and orientation) and the electrical transport properties of the same InAs NW: (1) fabricate a back-gate field effect transistor (FET) of a single InAs NW utilizing photoresist S1813 as the dielectric and perform all the room-temperature and low-temperature electrical measurements; (2) etch the photoresist under the channel by O_2 plasma treatment to make the NW suspended; and (3) transfer the suspended NW onto a holey carbon film supported by Cu grids with patterned marks for HRTEM investigation [130]. Besides, Figure 7a–c depicts a dual-beam scanning electron microscope (SEM) system, in which the electrical parameters are extracted through a tungsten tip connected with the top of the GaAs NW and the intrinsic interfaces are revealed by X-ray nanodiffraction (n-XRD) on the same NW using focused synchrotron radiation. By successively printing of GaAs NWs on LOR 3A resists, we obtained the high-density multilayer NW arrays for selected area electron diffraction (SAED), XRD characterizations and subsequent measurement of PV properties [132]. The results in Figure 7d–f show that the open-circuit voltage of purely <111>-oriented NW arrayed cells is far higher than that of <110>-oriented NW arrayed counterparts, suggesting the careful NW design considerations for achieving optimal PV performances [131].

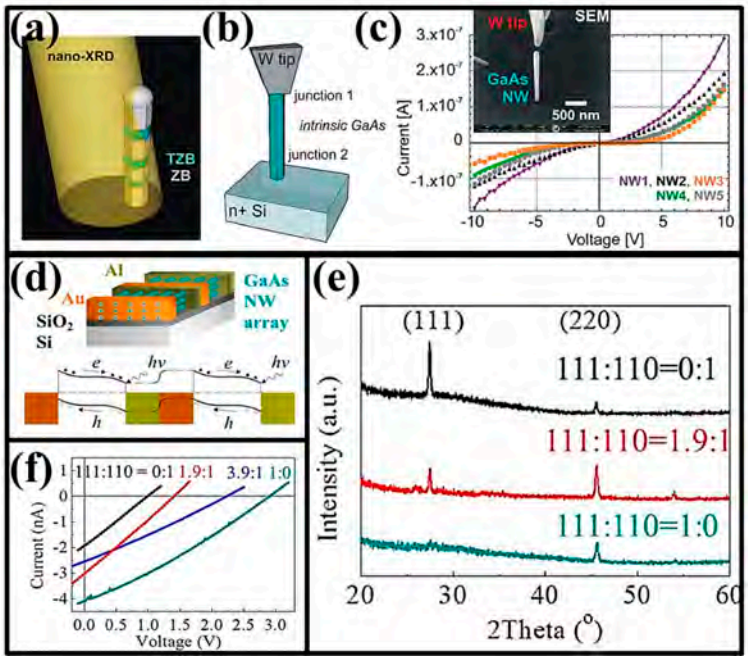

Figure 7. Correlation of structure and properties of GaAs NWs. (**a**–**c**) In situ measurement of the as-grown individual GaAs NW within a dual-beam SEM system. The I–V characteristics of selected NWs were measured through a tungsten tip brought into contact with the top of the NW, whereas the structural information was revealed by n-XRD on the same NW using focused synchrotron radiation. (**d**–**f**) Crystal orientation controlled PV properties of multilayer GaAs NW arrays. (**d**) Schematic illustration of the PV device structure and the corresponding energy band diagram. (**e**) XRD patterns collected of the three-layer GaAs NW parallel arrays. The growth directions of NWs were evaluated by XRD before the fabrication of corresponding parallel NW array based Schottky PV devices. (**f**) The PV performance fabricated with different mixing ratios of <111>- and <110>-oriented NWs. Adapted with permission from [131,132].

4. Optical Absorption

For the bulk-like PV devices, the absorption of light is generally proportional to the linear absorption coefficient and the material thickness predicted from the Lambert-Beer law [10]. However, it turns to be a complex phenomenon for NW-based solar cells, in which the material size is limited to wavelength-scale dimensions. On one hand, strong optical resonance effects have been observed in the elastic scattering, light emission, and Raman measurements on metallic NPs and dielectric NWs near natural frequencies of oscillation [15,74,133]. It is found that the NWs act as dielectric cavities strongly confining light by leaky-mode resonances (LMRs) effects. Light trapping has been observed and measured in Si NW and InP NW solar cells, which attributes to an enhanced PCE exceeding the limit of simple ray optics [57,69]. Thus, the light absorption area is enhanced and usually larger than the physical cross-sectional projected area. The resonance absorption is highly dependent on the geometry (length and diameter) and crystal structure (orientation and phase) of NWs [133]. For example, Anttu optimized both the NW length and diameter in his analysis by combing the absorption and emission modeling [31]. Heiss and Morral simulated the light absorption and fundamental efficiency limits of a horizontal GaAs NW lying flat on a substrate, as shown in Figure 8a–c [73]. In general, the external quantum efficiency (EQE) of a solar cell refers to the efficiency of light-electricity conversion calculated by the incident light, while the internal quantum efficiency (IQE) corresponds to the one with respect to the absorbed light. For GaAs NW with the ideally reflecting metal substrate, the calculations in Figure 8c show that the ratio EQE/IQE can be ~1.1 due to Mie resonances, implying the light absorption in NWs is comparable with that in thin film counterparts [73]. Kempa et al. reported apparent EQE values (corresponding projected area) up to 2 for lying coaxial multishell NWs indicated in Figure 8e [72]. The overall built-in light concentration is significantly enhanced (~12) in solar cell based on a standing GaAs NW, as shown in Figure 8d,e [74]. Interestingly, an efficient multiterminal NW solar cell design with a theoretical conversion efficiency of 48.3% was achieved utilizing an efficient lateral spectrum splitting between three different III/V NWs ($Al_{0.54}Ga_{0.46}As$, GaAs, $In_{0.37}Ga_{0.63}As$ NW with the radii (length) of 51 nm (12 μm), 73 nm (6.6 μm), and 114 nm (3.3 μm) grown on a flat silicon substrate [134].

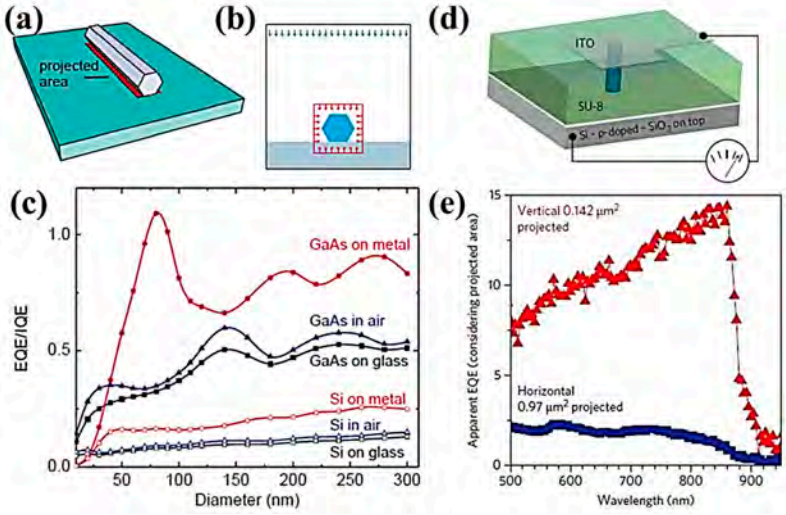

Figure 8. Simulated and experimental light absorption of a horizontal and vertical GaAs NW. (**a**,**b**) Sketch of the simulated GaAs NW lying on a planar substrate and the 2D-simulation geometry. (**c**) The external quantum efficiency (EQE)/internal quantum efficiency (IQE) ratio of GaAs NW in dependence of NW diameter. (**d**) Schematic of the vertical single GaAs NW based solar cell. (**e**) EQE (normalized by indicated projected area) for both horizontal and vertical GaAs NW solar cell. Adapted with permission from [72–74].

On the other hand, NWs exhibit distinguished anti-reflection effect, which is important in maximizing the absorption of incident sunlight. This helps a lot in the reduction of production cost, as NW PVs do not require additional expensive anti-reflection layer. For example, different types of 1D Si nanostructures have been designed and developed by Johnny and his group, such as nanopillars, nanorods, nanopencils, nanocones, and others by wet chemical etching method, in order to integrate active PV structures with anti-reflection functionality [135]. Mariani et al. obtained the maximization of the optical absorption by simulating four different tiling patterns of GaAs nanopillar arrays [77]. Almost perfect absorption of light (higher than 97%) occurred in arrays of base-tapered InP NWs, which emphasized the influence of the NW geometry on the light absorption [135]. All these results demonstrate the advantage of light trapping in NW-based PV devices.

5. PV Device Fabrication and Performances

Generally, a photovoltaic device needs a p-n junction or a Schottky barrier to separate the photo induced electron/holes. For example, PV devices based on p-type/intrinsic/n-type (p-i-n) doped InP NWs were specially designed to reduce junction current leakage [69]. Axial p-i-n type single crystal Si NWs were also synthesized, which highlight unique opportunities for planar NW PV device [136]. GaP/GaAsP/GaP core-multishell segmented NWs were grown by the Au-catalyzed VLS process, which were expected to provide devices, monolithically integrated with Si microelectronics, with enhanced performance and functionality [137]. However, doping axial or radial p-n junction needs complex and sophisticated growth condition control, which would also necessitate complex device fabrication by well contacting the p and n region by the electrodes [74,77,138]. On the contrary, Schottky type PVs devices are much easier by a direct growth of intrinsic NWs and asymmetric electrodes for the Schottky barrier. It should be noted that though ideal Schottky contact can be formed between the Au catalyst and the GaAs NW body, and Schottky type PV can also be fabricated on single NWs as shown in Figure 4, the device fabrication would be too complex by just contact nanometer size Au catalysts [122]. Therefore, thermally depositing asymmetric electrodes would be more portable for a Schottky PV. As shown in Figure 9, though there is sever Fermi level pinning effect, the Schottky barrier is still dependent on the work function difference of the two electrodes, with the maximum barrier of 0.3–0.4 V available for the Au–Al pairs (~1/3 of the work function difference between Au and Al, i.e., $5.1 - 4.2 = 0.9$ eV) [81]. The relatively alleviated Fermi level pinning is due to the relatively lower surface state density on the surface of <111> NWs, as compared with those of <110> ones. Then, by this asymmetric Schottky PV device design using the single crystalline GaAs NWs grown by catalyst engineering, the single NW based Schottky PV has a high PCE of 16%. To enhance the output, the GaAs NWs can be contact printed into an array on Si, plastic, and glass substrates, with several cells connecting in tandem and in parallel as shown in Figure 9c–f.

The recent development of GaAs NW based PV is summarized in Table 1. It is clear that the single crystal GaAs NW synthesized by the catalyst epitaxy growth method can minimize the crystal defect, which is essential for the long minority lifetime for effective separation of the photo generated electron/holes. Generally, the electron lifetime (τ) of GaAs lies in the range of 10–100 ps, and electron mobility (μ) in the order of 4000 cm^2/Vs [139]. Therefore, the diffusion length can be estimated to be about 1 μm by the equation $(\mu\tau kT/e)^{1/2}$, where kT/e is the constant. This relatively long diffusion pathway make sure that most of the photo generated electron/holes can be effectively separated by the Schottky barrier, leading to high short circuit current and high conversion efficiency.

Many challenges still exist in making NW based PV devices. First, cost-effective and simple methods are still required to grow high quality NWs with regular crystal structure (growth directions, crystal phase, and polarity) and minimal defects. Second, controlled doping for p-n or p-i-n junctions as well as surface passivation techniques are needed to improve the separation and collection of carriers. Third, it is still lack of effective technique to removal of catalyst droplet to avoid reflection loss and the contamination of foreign-metals, particularly Au. This limits the integration of NW PV devices with current silicon electronic platforms. Fourth, low resistance contacts are necessary for

high performance tunnel junctions. For example, the surface Fermi-level pining makes the fabrication of efficient NW junction difficult. Finally, the reliability and long-term stability are also major issues that hinder the marketization of nanostructured PV devices. Most of the reported NW PV devices were fabricated and measured at the lab scale under different conditions (atmosphere, temperature, humidity, light source, etc.). Despite all these difficulties, we believe that the potential benefits of nanostructured PV device make it worth the continual efforts.

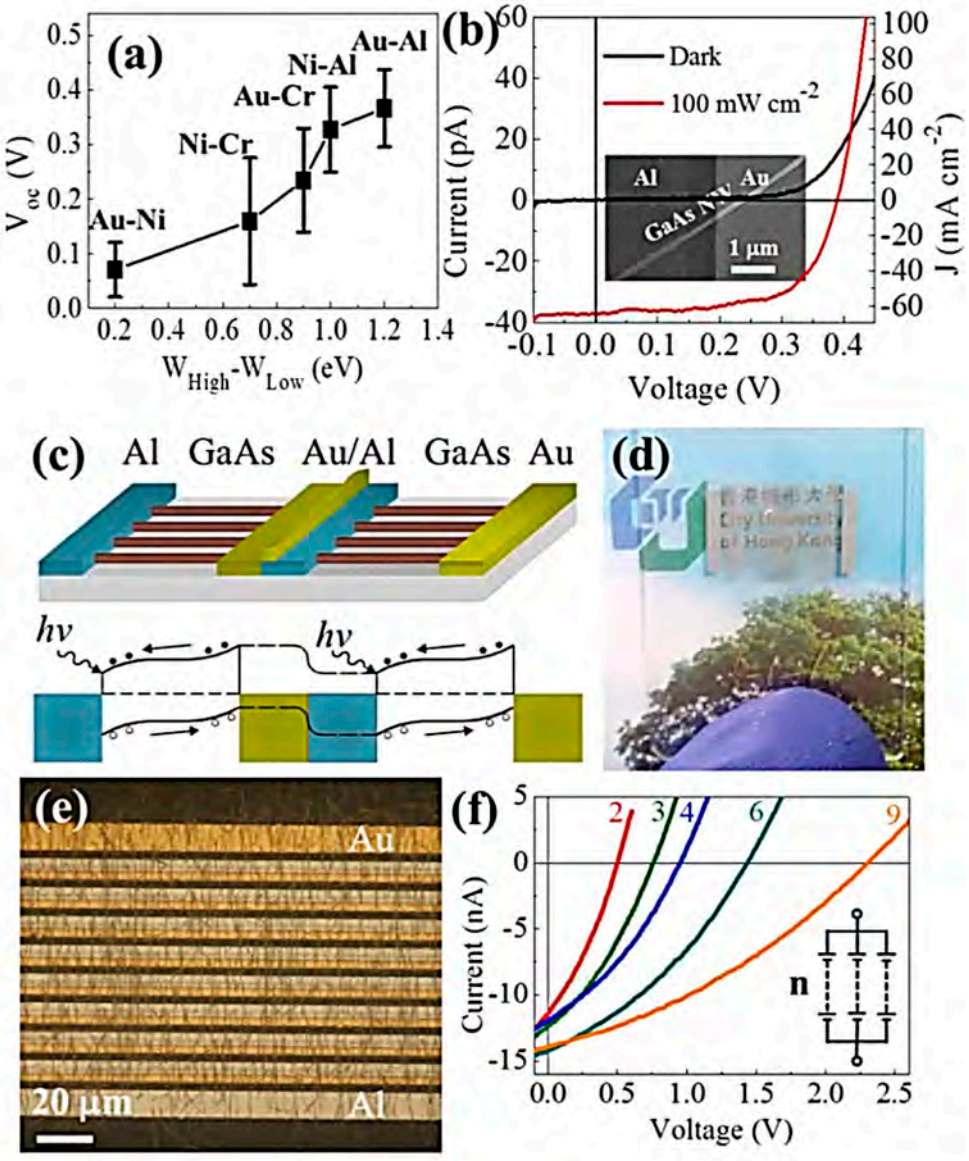

Figure 9. Structure and characteristics of transparent GaAs NW and NW array Schottky photovoltaic devices. (**a**) Open circuit voltage dependence on the work function difference of the asymmetric Schottky electrodes, (**b**) IV curves of one typical GaAs NW PV device, (**c**) schematic of cascaded GaAs NW device structure and band diagram, (**d**) optical microscope image showing a real test tandem (nine-cell connected in parallel) photovoltaic device, (**e**) photograph showing the optical transparency of the NW device constructed on glass, (**f**) I–V curves of the transparent photovoltaic devices composed of two, three, four, six, and nine cells in parallel. Adapted with permission from [81].

Table 1. Summary of GaAs and other NW-based PVs performance reported in recent literatures.

Type	Substrate	Method	Junction	Structure	PCE *	Ref.
GaAs NW	noncrystalline	catalyst epitaxy, CVD	Schottky contact	horizontal	16% [a]	[81]
GaAs NW	GaAs(111)	self-assisted MBE	radial p-i-n	horizontal	4.5% [a]	[78]
GaAs NW	GaAs(111)	MOCVD	GaAs NW/graphene	horizontal	8.8% [a]	[68]
GaAs NW	Si(111)	MBE	radial p-i-n	vertical	40% [a]	[74]
GaAs NW array	p-GaAs(111)B	SA-MOVPE	radial p-n	vertical	2.54%	[75]
GaAs NW array	p+ Si(111)	SA-MOVPE	axial n-i-p on Si	vertical	11.4%	[70]
GaAs NW array	p-GaAs(111)B	MOVPE, Au	axial p-i-n	vertical	15.3%	[140]
GaAs NW array	GaAs(111)	MOCVD	radial p-n, InGaP cap	vertical	6.63%	[77]
GaAs NW array	GaAs(100)	etched	GaAs/PEDOT:PSS	vertical	9.2%	[141]
GaAsP NW	Si(111)	MBE	radial p-n	horizontal	10.2%	[76]
InP NW array	p-InP	MOCVD	axial p-i-n	vertical	13.8%	[69]
Si NW	p-Si(111)	CVD	axial p-i-n	vertical	9%	[142]
GaAs sheets	GaAs(100)	MOCVD	planar p-n	vertical	14.5%	[56]

Abbreviations: PCE—power conversion efficiency; MBE—molecular beam epitaxy; MOCVD—metal organic chemical vapor deposition; MOVPE—metal organic vapor phase epitaxy; SA—selective area; Ga—gallium catalyzed; Au—gold catalyzed. * Performance parameters were measured at 1 Sun, AM1.5G illumination. [a] Apparent efficiency normalized to the projection area of the single NW, i.e., PCE = $[(V_{OC} \times I_{SC} \times FF)/(100\ mW/cm^2 \times \text{diameter} \times \text{active length})] \times 100\%$.

6. Conclusions and Remarks

In contrast with the selective epitaxy growth of III/V NWs on single crystalline substrate in traditional molecular beam epitaixy, the catalyst epitaxy growth route adopts the metal nanoparticle alloy as the growth model to lead to NW growth. In this growth method, NW stacking planes are well registered to the catalyst, with minimized lattice mismatch between catalyst/NW interfaces. In this way, NW morphology, growth orientations, crystal defects, etc. can be well tuned by the catalyst engineering such as catalyst metal, binary alloy composition, temperature profile, etc. The minimized crystal defects ensure long minority lifetime and the optimized orientation favors Schottky barrier fabrication with asymmetric metal electrodes. All these enhance the photo to electricity conversion efficiency to 16% of horizontal single GaAs NW PVs, promising for high efficiency and low cost solar cells.

Author Contributions: Y.W., X.Z., and N.H. performed the related experiments and analyzed the data; Z.Y., F.W., N.H., Y.C., and J.C.H. contributed to analysis tools; Y.W. and N.H. wrote the paper.

Funding: This work was supported by the National Natural Science Foundation of China (61504151 and 51602314), the National Key R&D Program of China (2016YFC0207100), the CAS-CSIRO project of the Bureau of International Co-operation of Chinese Academy of Sciences (122111KYSB20150064), and the State Key Laboratory of Multiphase Complex Systems (MPCS-2014-C-01).

Acknowledgments: The authors would like to thank for the financially supported by the National Natural Science Foundation of China (61504151 and 51602314), the National Key R&D Program of China (2016YFC0207100), the CAS-CSIRO project of the Bureau of International Co-operation of Chinese Academy of Sciences (122111KYSB20150064), and the State Key Laboratory of Multiphase Complex Systems (MPCS-2014-C-01).

Conflicts of Interest: The authors declare no conflict of interest.

References

1. Lohse, C. Environmental impact by hydrogeothermal energy generation in low-enthalpy regions. *Renew. Energy* **2018**, *128*, 509–519. [CrossRef]
2. Cao, X.H.; Tan, C.L.; Zhang, X.; Zhao, W.; Zhang, H. Solution-processed two-dimensional metal dichalcogenide-based nanomaterials for energy storage and conversion. *Adv. Mater.* **2016**, *28*, 6167–6196. [CrossRef] [PubMed]
3. Chu, S.; Majumdar, A. Opportunities and challenges for a sustainable energy future. *Nature* **2012**, *488*, 294–303. [CrossRef] [PubMed]
4. Lewis, N.S. Toward cost-effective solar energy use. *Science* **2007**, *315*, 798–801. [CrossRef] [PubMed]
5. Petrov, O.; Bi, X.T.; Lau, A. Impact assessment of biomass-based district heating systems in densely populated communities. Part II: Would the replacement of fossil fuels improve ambient air quality and human health? *Atmos. Environ.* **2017**, *161*, 191–199. [CrossRef]

6. Hidy, G.M. Multiscale impact of fuel consumption on air quality. *Energy Fuels* **2002**, *16*, 270–281. [CrossRef]
7. Poizot, P.; Dolhem, F. Clean energy new deal for a sustainable world: From non-CO_2 generating energy sources to greener electrochemical storage devices. *Energy Environ. Sci.* **2011**, *4*, 2003–2019. [CrossRef]
8. Zhou, H.L.; Qu, Y.Q.; Zeid, T.; Duan, X.F. Towards highly efficient photocatalysts using semiconductor nanoarchitectures. *Energy Environ. Sci.* **2012**, *5*, 6732–6743. [CrossRef]
9. Chen, J.; Huang, Y.; Zhang, N.N.; Zou, H.Y.; Liu, R.Y.; Tao, C.Y.; Fan, X.; Wang, Z.L. Micro-cable structured textile for simultaneously harvesting solar and mechanical energy. *Nat. Energy* **2016**, *1*, 16138. [CrossRef]
10. Han, N.; Yang, Z.X.; Shen, L.F.; Lin, H.; Wang, Y.; Pun, E.Y.B.; Chen, Y.F.; Ho, J.C. Design and fabrication of 1-D semiconductor nanomaterials for high-performance photovoltaics. *Sci. Bull.* **2016**, *61*, 357–367. [CrossRef]
11. LaPierre, R.R.; Chia, A.C.E.; Gibson, S.J.; Haapamaki, C.M.; Boulanger, J.; Yee, R.; Kuyanov, P.; Zhang, J.; Tajik, N.; Jewell, N.; et al. III-V nanowire photovoltaics: Review of design for high efficiency. *Phys. Status Solidi-R.* **2013**, *7*, 815–830. [CrossRef]
12. Beard, M.C.; Luther, J.M.; Nozik, A.J. The promise and challenge of nanostructured solar cells. *Nat. Nanotechnol.* **2014**, *9*, 951–954. [CrossRef] [PubMed]
13. Beard, M.C.; Luther, J.M.; Semonin, O.E.; Nozik, A.J. Third generation photovoltaics based on multiple exciton generation in quantum confined semiconductors. *Acc. Chem. Res.* **2013**, *46*, 1252–1260. [CrossRef] [PubMed]
14. Green, M.A. The path to 25% silicon solar cell efficiency: History of silicon cell evolution. *Prog. Photovolt.* **2009**, *17*, 183–189. [CrossRef]
15. Polman, A.; Atwater, H.A. Photonic design principles for ultrahigh-efficiency photovoltaics. *Nat. Mater.* **2012**, *11*, 174–177. [CrossRef] [PubMed]
16. Conibeer, G. Third-generation photovoltaics. *Mater. Today* **2007**, *10*, 42–50. [CrossRef]
17. Cao, F.; Chen, K.X.; Zhang, J.J.; Ye, X.Y.; Li, J.J.; Zou, S.; Su, X.D. Next-generation multi-crystalline silicon solar cells: Diamond-wire sawing, nano-texture and high efficiency. *Sol. Energy Mater. Sol. C* **2015**, *141*, 132–138. [CrossRef]
18. Placzek-Popko, E. Top PV market solar cells 2016. *Opto-Electron. Rev.* **2017**, *25*, 55–64. [CrossRef]
19. Spinelli, P.; Ferry, V.E.; van de Groep, J.; van Lare, M.; Verschuuren, M.A.; Schropp, R.E.I.; Atwater, H.A.; Polman, A. Plasmonic light trapping in thin-film Si solar cells. *J. Opt.* **2012**, *14*, 024002. [CrossRef]
20. Lee, T.D.; Ebong, A.U. A review of thin film solar cell technologies and challenges. *Renew. Sustain. Energy Rev.* **2017**, *70*, 1286–1297. [CrossRef]
21. Gowrishankar, V.; Luscombe, C.K.; McGehee, M.D.; Frechet, J.M.J. High-efficiency, Cd-free copper-indium-gallium-diselenide/polymer hybrid solar cells. *Sol. Energy Mater. Sol. C* **2007**, *91*, 807–812. [CrossRef]
22. Bhattacharya, R.N. CIGS-based solar cells prepared from electrodeposited stacked Cu/In/Ga layers. *Sol. Energy Mater. Sol. C* **2013**, *113*, 96–99. [CrossRef]
23. Avrutin, V.; Izyumskaya, N.; Morkoc, H. Semiconductor solar cells: Recent progress in terrestrial applications. *Superlattices Microstruct.* **2011**, *49*, 337–364. [CrossRef]
24. Greenaway, A.L.; Boucher, J.W.; Oener, S.Z.; Funch, C.J.; Boettcher, S.W. Low-Cost Approaches to III-V Semiconductor Growth for Photovoltaic Applications. *ACS Energy Lett.* **2017**, *2*, 2270–2282. [CrossRef]
25. Shockley, W.; Queisser, H.J. Detailed balance limit of efficiency of p-n junction solar cells. *J. Appl. Phys.* **1961**, *32*, 510–519. [CrossRef]
26. Green, M.A. Analytical treatment of Trivich-Flinn and Shockley-Queisser photovoltaic efficiency limits using polylogarithms. *Prog. Photovolt.* **2012**, *20*, 127–134. [CrossRef]
27. Mann, S.A.; Grote, R.R.; Osgood, R.M.; Alu, A.; Garneet, E.C. Opportunities and Limitations for Nanophotonic Structures to Exceed the Shockley-Queisser Limit. *ACS Nano* **2016**, *10*, 8620–8631. [CrossRef] [PubMed]
28. Yu, Z.F.; Sandhu, S.; Fan, S.H. Efficiency above the Shockley-Queisser Limit by using nanophotonic effects to create multiple effective bandgaps with a single semiconductor. *Nano Lett.* **2014**, *14*, 66–70. [CrossRef] [PubMed]
29. Rao, A.; Friend, R.H. Harnessing singlet exciton fission to break the Shockley-Queisser limit. *Nat. Rev. Mater.* **2017**, *2*, 17063. [CrossRef]
30. Brown, G.F.; Wu, J.Q. Third generation photovoltaics. *Laser Photonics Rev.* **2009**, *3*, 394–405. [CrossRef]
31. Anttu, N. Shockley-Queisser Detailed Balance Efficiency Limit for Nanowire Solar Cells. *ACS Photonics* **2015**, *2*, 446–453. [CrossRef]

32. Davis, N.; Bohm, M.L.; Tabachnyk, M.; Wisnivesky-Rocca-Rivarola, F.; Jellicoe, T.C.; Ducati, C.; Ehrler, B.; Greenham, N.C. Multiple-exciton generation in lead selenide nanorod solar cells with external quantum efficiencies exceeding 120%. *Nat. Commun.* **2015**, *6*, 8259. [CrossRef] [PubMed]
33. Devos, A. Detailed balance limit of the efficiency of tandem solar-cells. *J. Phys. D Appl. Phys.* **1980**, *13*, 839–846.
34. Choi, J.J.; Wenger, W.N.; Hoffman, R.S.; Lim, Y.-F.; Luria, J.; Jasieniak, J.; Marohn, J.A.; Hanrath, T. Solution-processed nanocrystal quantum dot tandem solar cells. *Adv. Mater.* **2011**, *23*, 3144–3148. [CrossRef] [PubMed]
35. Wang, X.; Koleilat, G.I.; Tang, J.; Liu, H.; Kramer, I.J.; Debnath, R.; Brzozowski, L.; Barkhouse, D.A.R.; Levina, L.; Hoogland, S.; et al. Tandem colloidal quantum dot solar cells employing a graded recombination layer. *Nat. Photonics* **2011**, *5*, 480–484. [CrossRef]
36. Green, M.A.; Emery, K.; Hishikawa, Y.; Warta, W.; Dunlop, E.D. Solar cell efficiency tables (version 44). *Prog. Photovolt.* **2014**, *22*, 701–710. [CrossRef]
37. Xue, Q.F.; Xia, R.X.; Brabec, C.J.; Yip, H.L. Recent advances in semi-transparent polymer and perovskite solar cells for power generating window applications. *Energy Environ. Sci.* **2018**, *11*, 1688–1709. [CrossRef]
38. Zhao, B.D.; Abdi-Jalebi, M.; Tabachnyk, M.; Glass, H.; Kamboj, V.S.; Nie, W.Y.; Pearson, A.J.; Puttisong, Y.; Godel, K.C.; Beere, H.E.; et al. High open-circuit voltages in tin-rich low-bandgap perovskite-based planar heterojunction photovoltaics. *Adv. Mater.* **2017**, *29*, 1604744. [CrossRef] [PubMed]
39. Nozik, A.J. Spectroscopy and hot electron relaxation dynamics in semiconductor quantum wells and quantum dots. *Annu. Rev. Phys. Chem.* **2001**, *52*, 193–231. [CrossRef] [PubMed]
40. Beard, M.C.; Midgett, A.G.; Law, M.; Semonin, O.E.; Ellingson, R.J.; Nozik, A.J. Variations in the quantum efficiency of multiple exciton generation for a series of chemically treated pbse nanocrystal films. *Nano Lett.* **2009**, *9*, 836–845. [CrossRef] [PubMed]
41. Cirloganu, C.M.; Padilha, L.A.; Lin, Q.; Makarov, N.S.; Velizhanin, K.A.; Luo, H.; Robel, I.; Pietryga, J.M.; Klimov, V.I. Enhanced carrier multiplication in engineered quasi-type-II quantum dots. *Nat. Commun.* **2014**, *5*, 4148. [CrossRef] [PubMed]
42. Nozik, A.J. Quantum dot solar cells. *Phys. E Low Dimens. Syst. Nanostruct.* **2002**, *14*, 115–120. [CrossRef]
43. Jia, Y.; Wei, J.Q.; Wang, K.L.; Cao, A.Y.; Shu, Q.K.; Gui, X.C.; Zhu, Y.Q.; Zhuang, D.M.; Zhang, G.; Ma, B.B.; et al. Nanotube-silicon heterojunction solar cells. *Adv. Mater.* **2008**, *20*, 4594–4598. [CrossRef]
44. Chen, T.; Wang, S.T.; Yang, Z.B.; Feng, Q.Y.; Sun, X.M.; Li, L.; Wang, Z.S.; Peng, H.S. Flexible, light-weight, ultrastrong, and semiconductive carbon nanotube fibers for a highly efficient solar cell. *Angew. Chem. Int. Ed.* **2011**, *50*, 1815–1819. [CrossRef] [PubMed]
45. Mir, N.; Lee, K.; Paramasivam, I.; Schmuki, P. Optimizing TiO_2 nanotube top geometry for use in dye-sensitized solar cells. *Chem. Eur. J.* **2012**, *18*, 11862–11866. [CrossRef] [PubMed]
46. Liu, J.; Yi, F.T.; Wang, B.; Zhang, T.C.; Wang, Y.T.; Zhou, Y. Fabrication and photovoltaic effect of cds/silicon nanopillars heterojunction solar cell. *ChemistrySelect* **2016**, *1*, 4901–4905. [CrossRef]
47. Sealy, C. Nanopillars could spell cheaper, more efficient solar cells. *Nano Today* **2009**, *4*, 379.
48. Sun, H.; Ren, F.; Ng, K.W.; Tran, T.T.D.; Li, K.; Chang-Hasnain, C.J. Nanopillar lasers directly grown on silicon with heterostructure surface passivation. *ACS Nano* **2014**, *8*, 6833–6839. [CrossRef] [PubMed]
49. Baxter, J.B.; Aydil, E.S. Nanowire-based dye-sensitized solar cells. *Appl. Phys. Lett.* **2005**, *86*, 053114. [CrossRef]
50. Tsakalakos, L.; Balch, J.; Fronheiser, J.; Korevaar, B.A.; Sulima, O.; Rand, J. Silicon nanowire solar cells. *Appl. Phys. Lett.* **2007**, *91*, 233117. [CrossRef]
51. Garnett, E.C.; Yang, P. Silicon nanowire radial p-n junction solar cells. *J. Am. Chem. Soc.* **2008**, *130*, 9224–9225. [CrossRef] [PubMed]
52. Garnett, E.; Yang, P. Light trapping in silicon nanowire solar cells. *Nano Lett.* **2010**, *10*, 1082–1087. [CrossRef] [PubMed]
53. Kelzenberg, M.D.; Boettcher, S.W.; Petykiewicz, J.A.; Turner-Evans, D.B.; Putnam, M.C.; Warren, E.L.; Spurgeon, J.M.; Briggs, R.M.; Lewis, N.S.; Atwater, H.A. Enhanced absorption and carrier collection in Si wire arrays for photovoltaic applications. *Nat. Mater.* **2010**, *9*, 239–244. [CrossRef] [PubMed]
54. Borgstrom, M.T.; Wallentin, J.; Heurlin, M.; Falt, S.; Wickert, P.; Leene, J.; Magnusson, M.H.; Deppert, K.; Samuelson, L. Nanowires with promise for photovoltaics. *IEEE J. Sel. Top. Quantum Electron.* **2011**, *17*, 1050–1061. [CrossRef]

55. Peng, K.-Q.; Lee, S.-T. Silicon nanowires for photovoltaic solar energy conversion. *Adv. Mater.* **2011**, *23*, 198–215. [CrossRef] [PubMed]
56. Wang, Y.; Yang, Z.X.; Wu, X.F.; Han, N.; Liu, H.Y.; Wang, S.B.; Li, J.; Tse, W.; Yip, S.; Chen, Y.F.; et al. Growth and photovoltaic properties of high-quality gaas nanowires prepared by the two-source CVD method. *Nanoscale Res. Lett.* **2016**, *11*, 191. [CrossRef] [PubMed]
57. Yoon, J.; Jo, S.; Chun, I.S.; Jung, I.; Kim, H.-S.; Meitl, M.; Menard, E.; Li, X.; Coleman, J.J.; Paik, U.; et al. GaAs photovoltaics and optoelectronics using releasable multilayer epitaxial assemblies. *Nature* **2010**, *465*, 329. [CrossRef] [PubMed]
58. Han, N.; Wang, F.; Yip, S.; Hou, J.J.; Xiu, F.; Shi, X.; Hui, A.T.; Hung, T.; Ho, J.C. GaAs nanowire Schottky barrier photovoltaics utilizing Au-Ga alloy catalytic tips. *Appl. Phys. Lett.* **2012**, *101*, 013105. [CrossRef]
59. Otnes, G.; Borgstrom, M.T. Towards high efficiency nanowire solar cells. *Nano Today* **2017**, *12*, 31–45. [CrossRef]
60. Yao, M.; Huang, N.; Cong, S.; Chi, C.-Y.; Seyedi, M.A.; Lin, Y.-T.; Cao, Y.; Povinelli, M.L.; Dapkus, P.D.; Zhou, C. GaAs Nanowire array solar cells with axial p-i-n junctions. *Nano Lett.* **2014**, *14*, 3293–3303. [CrossRef] [PubMed]
61. Afshar, E.N.; Xosrovashvili, G.; Rouhi, R.; Gorji, N.E. Review on the application of nanostructure materials in solar cells. *Mod. Phys. Lett. B* **2015**, *29*, 1550118. [CrossRef]
62. Aberg, I.; Vescovi, G.; Asoli, D.; Naseem, U.; Gilboy, J.P.; Sundvall, C.; Dahlgren, A.; Svensson, K.E.; Anttu, N.; Bjork, M.T.; et al. A GaAs nanowire array solar cell with 15.3% efficiency at 1 sun. *IEEE J. Photovolt.* **2016**, *6*, 185–190. [CrossRef]
63. Yu, S.; Witzigmann, B. A high efficiency dual-junction solar cell implemented as a nanowire array. *Opt. Express* **2013**, *21*, A167–A172. [CrossRef] [PubMed]
64. Im, J.-H.; Luo, J.; Franckevicius, M.; Pellet, N.; Gao, P.; Moehl, T.; Zakeeruddin, S.M.; Nazeeruddin, M.K.; Graetzel, M.; Park, N.-G. Nanowire perovskite solar cell. *Nano Lett.* **2015**, *15*, 2120–2126. [CrossRef] [PubMed]
65. Wang, Y.; Zhang, Y.; Zhang, D.; He, S.; Li, X. Design high-efficiency III-V nanowire/Si two-junction solar cell. *Nanoscale Res. Lett.* **2015**, *10*, 269. [CrossRef] [PubMed]
66. Wu, S.-H.; Povinelli, M.L. Solar heating of GaAs nanowire solar cells. *Opt. Express* **2015**, *23*, A1363–A1372. [CrossRef] [PubMed]
67. Boulanger, J.P.; Chia, A.C.E.; Wood, B.; Yazdi, S.; Kasama, T.; Aagesen, M.; LaPierre, R.R. Characterization of a Ga-Assisted GaAs Nanowire Array Solar Cell on Si Substrate. *IEEE J. Photovolt.* **2016**, *6*, 661–667. [CrossRef]
68. Luo, Y.B.; Yan, X.; Zhang, J.N.; Li, B.; Wu, Y.; Lu, Q.C.; Jin, C.X.S.; Zhang, X.; Ren, X.M. A graphene/single GaAs nanowire Schottky junction photovoltaic device. *Nanoscale* **2018**, *10*, 9212–9217. [CrossRef] [PubMed]
69. Wallentin, J.; Anttu, N.; Asoli, D.; Huffman, M.; Aberg, I.; Magnusson, M.H.; Siefer, G.; Fuss-Kailuweit, P.; Dimroth, F.; Witzigmann, B.; et al. InP nanowire array solar cells achieving 13.8% efficiency by exceeding the ray optics limit. *Science* **2013**, *339*, 1057–1060. [CrossRef] [PubMed]
70. Yao, M.; Cong, S.; Arab, S.; Huang, N.; Povinelli, M.L.; Cronin, S.B.; Dapkus, P.D.; Zhou, C. Tandem solar cells using gaas nanowires on Si: Design, fabrication, and observation of voltage addition. *Nano Lett.* **2015**, *15*, 7217–7224. [CrossRef] [PubMed]
71. Atwater, H.A.; Polman, A. Plasmonics for improved photovoltaic devices. *Nat. Mater.* **2010**, *9*, 205–213. [CrossRef] [PubMed]
72. Kempa, T.J.; Cahoon, J.F.; Kim, S.-K.; Day, R.W.; Bell, D.C.; Park, H.-G.; Lieber, C.M. Coaxial multishell nanowires with high-quality electronic interfaces and tunable optical cavities for ultrathin photovoltaics. *Proc. Natl. Acad. Sci. USA* **2012**, *109*, 1407–1412. [CrossRef] [PubMed]
73. Heiss, M.; Morral, A.F.I. Fundamental limits in the external quantum efficiency of single nanowire solar cells. *Appl. Phys. Lett.* **2011**, *99*, 263102. [CrossRef]
74. Krogstrup, P.; Jorgensen, H.I.; Heiss, M.; Demichel, O.; Holm, J.V.; Aagesen, M.; Nygard, J.; Morral, A.F.I. Single-nanowire solar cells beyond the Shockley-Queisser limit. *Nat. Photonics* **2013**, *7*, 306–310. [CrossRef]
75. Mariani, G.; Wong, P.S.; Katzenmeyer, A.M.; Leonard, F.; Shapiro, J.; Huffaker, D.L. Patterned radial GaAs nanopillar solar cells. *Nano Lett.* **2011**, *11*, 2490–2494. [CrossRef] [PubMed]
76. Holm, J.V.; Jorgensen, H.I.; Krogstrup, P.; Nygard, J.; Liu, H.; Aagesen, M. Surface-passivated GaAsP single-nanowire solar cells exceeding 10% efficiency grown on silicon. *Nat. Commun.* **2013**, *4*, 1498. [CrossRef] [PubMed]

77. Mariani, G.; Scofield, A.C.; Hung, C.H.; Huffaker, D.L. GaAs nanopillar-array solar cells employing in situ surface passivation. *Nat. Commun.* **2013**, *4*, 1497. [CrossRef] [PubMed]
78. Colombo, C.; Heiss, M.; Graetzel, M.; Fontcuberta i Morral, A. Gallium arsenide p-i-n radial structures for photovoltaic applications. *Appl. Phys. Lett.* **2009**, *94*, 173108. [CrossRef]
79. Schubert, M.B.; Werner, J.H. Flexible solar cells for clothing. *Mater. Today* **2006**, *9*, 42–50. [CrossRef]
80. Fan, Z.; Razavi, H.; Do, J.-W.; Moriwaki, A.; Ergen, O.; Chueh, Y.-L.; Leu, P.W.; Ho, J.C.; Takahashi, T.; Reichertz, L.A.; et al. Three-dimensional nanopillar-array photovoltaics on low-cost and flexible substrates. *Nat. Mater.* **2009**, *8*, 648–653. [CrossRef] [PubMed]
81. Han, N.; Yang, Z.-X.; Wang, F.; Dong, G.; Yip, S.; Liang, X.; Hung, T.F.; Chen, Y.; Ho, J.C. High-performance GaAs nanowire solar cells for flexible and transparent photovoltaics. *ACS Appl. Mater. Interfaces* **2015**, *7*, 20454–20459. [CrossRef] [PubMed]
82. Wang, X.Y.; Du, W.N.; Yang, X.G.; Zhang, X.W.; Yang, T. Self-catalyzed growth mechanism of InAs nanowires and growth of InAs/GaSb heterostructured nanowires on Si substrates. *J. Cryst. Growth* **2015**, *426*, 287–292. [CrossRef]
83. Schroth, P.; Jakob, J.; Feigl, L.; Kashani, S.M.M.; Vogel, J.; Strempfer, J.; Keller, T.F.; Pietsch, U.; Baumbach, T. Radial growth of self-catalyzed GaAs nanowires and the evolution of the liquid ga-droplet studied by time-resolved in situ X-ray diffraction. *Nano Lett.* **2018**, *18*, 101–108. [CrossRef] [PubMed]
84. Plissard, S.; Larrieu, G.; Wallart, X.; Caroff, P. High yield of self-catalyzed GaAs nanowire arrays grown on silicon via gallium droplet positioning. *Nanotechnology* **2011**, *22*, 275602. [CrossRef] [PubMed]
85. Tersoff, J. Stable self-catalyzed growth of III-V nanowires. *Nano Lett.* **2015**, *15*, 6609–6613. [CrossRef] [PubMed]
86. Dong, Z.N.; Andre, Y.; Dubrovskii, V.G.; Bougerol, C.; Leroux, C.; Ramdani, M.R.; Monier, G.; Trassoudaine, A.; Castelluci, D.; Gil, E. Self-catalyzed GaAs nanowires on silicon by hydride vapor phase epitaxy. *Nanotechnology* **2017**, *28*, 125602. [CrossRef] [PubMed]
87. Zi, Y.L.; Suslov, S.; Yang, C. Understanding self-catalyzed epitaxial growth of III-V Nanowires toward controlled synthesis. *Nano Lett.* **2017**, *17*, 1167–1173. [CrossRef] [PubMed]
88. Dubrovskii, V.G. Understanding the vapor-liquid-solid growth and composition of ternary III-V nanowires and nanowire heterostructures. *J. Phys. D Appl. Phys.* **2017**, *50*, 21. [CrossRef]
89. Krogstrup, P.; Jorgensen, H.I.; Johnson, E.; Madsen, M.H.; Sorensen, C.B.; Morral, A.F.I.; Aagesen, M.; Nygard, J.; Glas, F. Advances in the theory of III-V nanowire growth dynamics. *J. Phys. D Appl. Phys.* **2013**, *46*, 29. [CrossRef]
90. Zhou, C.; Zheng, K.; Lu, Z.Y.; Zhang, Z.; Liao, Z.M.; Chen, P.P.; Lu, W.; Zou, J. Quality control of GaAs nanowire structures by limiting as flux in molecular beam epitaxy. *J. Phys. Chem. C* **2015**, *119*, 20721–20727. [CrossRef]
91. Yang, X.D.; Shu, H.B.; Liang, P.; Cao, D.; Chen, X.S. Crystal phase and facet effects on the structural stability and electronic properties of gap nanowires. *J. Phys. Chem. C* **2015**, *119*, 12030–12036. [CrossRef]
92. Han, N.; Yang, Z.X.; Wang, F.Y.; Yip, S.; Dong, G.F.; Liang, X.G.; Hung, T.F.; Chen, Y.F.; Ho, J.C. Modulating the morphology and electrical properties of gaas nanowires via catalyst stabilization by oxygen. *ACS Appl. Mater. Interfaces* **2015**, *7*, 5591–5597. [CrossRef] [PubMed]
93. Xu, H.Y.; Wang, Y.; Guo, Y.N.; Liao, Z.M.; Gao, Q.; Tan, H.H.; Jagadish, C.; Zou, J. Defect-free <110> zinc-blende structured inas nanowires catalyzed by palladium. *Nano Lett.* **2012**, *12*, 5744–5749. [CrossRef] [PubMed]
94. Han, N.; Wang, F.Y.; Hou, J.J.; Yip, S.; Lin, H.; Fang, M.; Xiu, F.; Shi, X.L.; Hung, T.F.; Ho, J.C. Manipulated growth of GaAs nanowires: Controllable crystal quality and growth orientations via a supersaturation-controlled engineering process. *Cryst. Growth Des.* **2012**, *12*, 6243–6249. [CrossRef]
95. Barrigon, E.; Hultin, O.; Lindgren, D.; Yadegari, F.; Magnusson, M.H.; Samuelson, L.; Johansson, L.I.M.; Bjork, M.T. GaAs nanowire pn-junctions produced by low-cost and high-throughput aerotaxy. *Nano Lett.* **2018**, *18*, 1088–1092. [CrossRef] [PubMed]
96. Metaferia, W.; Sivakumar, S.; Persson, A.R.; Geijselaers, I.; Wallenberg, L.R.; Deppert, K.; Samuelson, L.; Magnusson, M.H. n-type doping and morphology of GaAs nanowires in Aerotaxy. *Nanotechnology* **2018**, *29*, 8. [CrossRef] [PubMed]
97. Morales, A.M.; Lieber, C.M. A laser ablation method for the synthesis of crystalline semiconductor nanowires. *Science* **1998**, *279*, 208–211. [CrossRef] [PubMed]

98. Yang, Z.X.; Wang, F.Y.; Han, N.; Lin, H.; Cheung, H.Y.; Fang, M.; Yip, S.; Hung, T.F.; Wong, C.Y.; Ho, J.C. Crystalline GaSb nanowires synthesized on amorphous substrates: From the formation mechanism to p-channel transistor applications. *ACS Appl. Mater. Interfaces* **2013**, *5*, 10946–10952. [CrossRef] [PubMed]
99. Zhang, G.Q.; Tateno, K.; Sanada, H.; Tawara, T.; Gotoh, H.; Nakano, H. Synthesis of GaAs nanowires with very small diameters and their optical properties with the radial quantum-confinement effect. *Appl. Phys. Lett.* **2009**, *95*, 123104. [CrossRef]
100. Han, N.; Hui, A.T.; Wang, F.Y.; Hou, J.J.; Xiu, F.; Hung, T.F.; Ho, J.C. Crystal phase and growth orientation dependence of GaAs nanowires on NixGay seeds via vapor-solid-solid mechanism. *Appl. Phys. Lett.* **2011**, *99*, 083114. [CrossRef]
101. Han, N.; Wang, Y.; Yang, Z.X.; Yip, S.; Wang, Z.; Li, D.P.; Hung, T.F.; Wang, F.Y.; Chen, Y.F.; Ho, J.C. Controllable III-V nanowire growth via catalyst epitaxy. *J. Mater. Chem. C* **2017**, *5*, 4393–4399. [CrossRef]
102. Algra, R.E.; Vonk, V.; Wermeille, D.; Szweryn, W.J.; Verheijen, M.A.; van Enckevort, W.J.P.; Bode, A.A.C.; Noorduin, W.L.; Tancini, E.; de Jong, A.E.F.; et al. Formation of wurtzite InP nanowires explained by liquid-ordering. *Nano Lett.* **2011**, *11*, 44–48. [CrossRef] [PubMed]
103. Jam, R.J.; Heurlin, M.; Jain, V.; Kvennefors, A.; Graczyk, M.; Maximov, I.; Borgstrom, M.T.; Pettersson, H.; Samuelson, L. III-V Nanowire synthesis by use of electrodeposited gold particles. *Nano Lett.* **2015**, *15*, 134–138.
104. Jacobsson, D.; Lehmann, S.; Dick, K.A. Crystal structure tuning in GaAs nanowires using HCl. *Nanoscale* **2014**, *6*, 8257–8264. [CrossRef] [PubMed]
105. Chou, Y.C.; Hillerich, K.; Tersoff, J.; Reuter, M.C.; Dick, K.A.; Ross, F.M. Atomic-scale variability and control of III-V nanowire growth kinetics. *Science* **2014**, *343*, 281–284. [CrossRef] [PubMed]
106. Ikejiri, K.; Ishizaka, F.; Tomioka, K.; Fukui, T. GaAs nanowire growth on polycrystalline silicon thin films using selective-area MOVPE. *Nanotechnology* **2013**, *24*, 115304. [CrossRef] [PubMed]
107. Yang, T.; Hertenberger, S.; Morkoetter, S.; Abstreiter, G.; Koblmueller, G. Size, composition, and doping effects on In(Ga)As nanowire/Si tunnel diodes probed by conductive atomic force microscopy. *Appl. Phys. Lett.* **2012**, *101*, 233102. [CrossRef]
108. Dhaka, V.; Haggren, T.; Jussila, H.; Jiang, H.; Kauppinen, E.; Huhtio, T.; Sopanen, M.; Lipsanen, H. High quality GaAs nanowires grown on glass substrates. *Nano Lett.* **2012**, *12*, 1912–1918. [CrossRef] [PubMed]
109. Yuan, X.M.; Caroff, P.; Wong-Leung, J.; Fu, L.; Tan, H.H.; Jagadish, C. Tunable polarity in a III-V nanowire by droplet wetting and surface energy engineering. *Adv. Mater.* **2015**, *27*, 6096–6103. [CrossRef] [PubMed]
110. Han, N.; Wang, F.Y.; Hou, J.J.; Xiu, F.; Yip, S.; Hui, A.T.; Hung, T.F.; Ho, J.C. Controllable p-n switching behaviors of GaAs nanowires via an interface effect. *ACS Nano* **2012**, *6*, 4428–4433. [CrossRef] [PubMed]
111. Anttu, N.; Lehmann, S.; Storm, K.; Dick, K.A.; Samuelson, L.; Wu, P.M.; Pistol, M.E. Crystal phase-dependent nanophotonic resonances in InAs nanowire arrays. *Nano Lett.* **2014**, *14*, 5650–5655. [CrossRef] [PubMed]
112. Wirths, S.; Mayer, B.F.; Schmid, H.; Sousa, M.; Gooth, J.; Riel, H.; Moselund, K.E. Room-temperature lasing from monolithically integrated GaAs microdisks on silicon. *ACS Nano* **2018**, *12*, 2169–2175. [CrossRef] [PubMed]
113. Borg, M.; Schmid, H.; Moselund, K.E.; Signorello, G.; Gignac, L.; Bruley, J.; Breslin, C.; Das Kanungo, P.; Werner, P.; Riel, H. Vertical III-V nanowire device integration on Si(100). *Nano Lett.* **2014**, *14*, 1914–1920. [CrossRef] [PubMed]
114. Sanchez, A.M.; Gott, J.A.; Fonseka, H.A.; Zhang, Y.; Liu, H.; Beanland, R. Stable defects in semiconductor nanowires. *Nano Lett.* **2018**, *18*, 3081–3087. [CrossRef] [PubMed]
115. Hoang, T.B.; Moses, A.F.; Ahtapodov, L.; Zhou, H.; Dheeraj, D.L.; van Helvoort, A.T.J.; Fimland, B.O.; Weman, H. Engineering parallel and perpendicular polarized photoluminescence from a single semiconductor nanowire by crystal phase control. *Nano Lett.* **2010**, *10*, 2927–2933. [CrossRef] [PubMed]
116. Jancu, J.M.; Gauthron, K.; Largeau, L.; Patriarche, G.; Harmand, J.C.; Voisin, P. Type II heterostructures formed by zinc-blende inclusions in InP and GaAs wurtzite nanowires. *Appl. Phys. Lett.* **2010**, *97*, 041910. [CrossRef]
117. Zhang, Y.Y.; Fonseka, H.A.; Aagesen, M.; Gott, J.A.; Sanchez, A.M.; Wu, J.; Kim, D.; Jurczak, P.; Huo, S.G.; Liu, H.Y. Growth of pure zinc-blende GaAs(P) core-shell nanowires with highly regular morphology. *Nano Lett.* **2017**, *17*, 4946–4950. [CrossRef] [PubMed]

118. Yang, Z.X.; Liu, L.Z.; Yip, S.P.; Li, D.P.; Shen, L.F.; Zhou, Z.Y.; Han, N.; Hung, T.F.; Pun, E.Y.B.; Wu, X.L.; et al. Complementary metal oxide semiconductor-compatible, high-mobility, <111>-oriented GaSb nanowires enabled by vapor-solid-solid chemical vapor deposition. *ACS Nano* **2017**, *11*, 4237–4246. [CrossRef] [PubMed]
119. Zhang, Z.; Lu, Z.Y.; Chen, P.P.; Lu, W.; Zou, J. Defect-free zinc-blende structured InAs nanowires realized by in situ two V/III ratio growth in molecular beam epitaxy. *Nanoscale* **2015**, *7*, 12592–12597. [CrossRef] [PubMed]
120. Fortuna, S.A.; Li, X. Metal-catalyzed semiconductor nanowires: A review on the control of growth directions. *Semicond. Sci. Tech.* **2010**, *25*, 024005. [CrossRef]
121. Han, N.; Hou, J.J.; Wang, F.Y.; Yip, S.; Yen, Y.T.; Yang, Z.X.; Dong, G.F.; Hung, T.; Chueh, Y.L.; Ho, J.C. GaAs nanowires: From manipulation of defect formation to controllable electronic transport properties. *ACS Nano* **2013**, *7*, 9138–9146. [CrossRef] [PubMed]
122. Wang, Z.; Wang, Y.; Zhou, X.; Yang, Z.; Yin, Y.; Zhang, J.; Han, N.; Ho, J.C.; Chen, Y. Controlled growth of heterostructured Ga/GaAs nanowires with sharp schottky barrier. *Cryst. Growth Des.* **2018**, *18*, 4438–4444. [CrossRef]
123. Bar-Sadan, M.; Barthel, J.; Shtrikman, H.; Houben, L. Direct imaging of single au atoms within GaAs nanowires. *Nano Lett.* **2012**, *12*, 2352–2356. [CrossRef] [PubMed]
124. Breuer, S.; Pfüller, C.; Flissikowski, T.; Brandt, O.; Grahn, H.T.; Geelhaar, L.; Riechert, H. Suitability of Au- and self-assisted gaas nanowires for optoelectronic applications. *Nano Lett.* **2011**, *11*, 1276–1279. [CrossRef] [PubMed]
125. Sun, Y.G.; Xia, Y.N. Shape-controlled synthesis of gold and silver nanoparticles. *Science* **2002**, *298*, 2176–2179. [CrossRef] [PubMed]
126. Park, J.; Joo, J.; Kwon, S.G.; Jang, Y.; Hyeon, T. Synthesis of monodisperse spherical nanocrystals. *Angew. Chem. Int. Ed.* **2007**, *46*, 4630–4660. [CrossRef] [PubMed]
127. Grzelczak, M.; Perez-Juste, J.; Mulvaney, P.; Liz-Marzan, L.M. Shape control in gold nanoparticle synthesis. *Chem. Soc. Rev.* **2008**, *37*, 1783–1791. [CrossRef] [PubMed]
128. Xia, Y.N.; Xiong, Y.J.; Lim, B.; Skrabalak, S.E. Shape-controlled synthesis of metal nanocrystals: Simple chemistry meets complex physics? *Angew. Chem. Int. Ed.* **2009**, *48*, 60–103. [CrossRef] [PubMed]
129. Lin, P.A.; Liang, D.; Reeves, S.; Gao, X.P.A.; Sankaran, R.M. Shape-controlled au particles for InAs nanowire growth. *Nano Lett.* **2012**, *12*, 315–320. [CrossRef] [PubMed]
130. Fu, M.; Tang, Z.; Li, X.; Ning, Z.; Pan, D.; Zhao, J.; Wei, X.; Chen, Q. Crystal phase- and orientation-dependent electrical transport properties of InAs nanowires. *Nano Lett.* **2016**, *16*, 2478–2484. [CrossRef] [PubMed]
131. Han, N.; Yang, Z.X.; Wang, F.Y.; Yip, S.; Li, D.P.; Hung, T.F.; Chen, Y.F.; Ho, J.C. Crystal orientation controlled photovoltaic properties of multilayer gaas nanowire arrays. *ACS Nano* **2016**, *10*, 6283–6290. [CrossRef] [PubMed]
132. Bussone, G.; Schaefer-Eberwein, H.; Dimakis, E.; Biermanns, A.; Carbone, D.; Tahraoui, A.; Geelhaar, L.; Bolivar, P.H.; Schuelli, T.U.; Pietsch, U. Correlation of electrical and structural properties of single as-grown GaAs nanowires on Si (111) substrates. *Nano Lett.* **2015**, *15*, 981–989. [CrossRef] [PubMed]
133. Cao, L.; White, J.S.; Park, J.-S.; Schuller, J.A.; Clemens, B.M.; Brongersma, M.L. Engineering light absorption in semiconductor nanowire devices. *Nat. Mater.* **2009**, *8*, 643–647. [CrossRef] [PubMed]
134. Dorodnyy, A.; Alarcon-Llado, E.; Shklover, V.; Hafner, C.; Morral, A.F.I.; Leuthold, J. Efficient multiterminal spectrum splitting via a nanowire array solar cell. *ACS Photonics* **2015**, *2*, 1284–1288. [CrossRef] [PubMed]
135. Diedenhofen, S.L.; Janssen, O.T.A.; Grzela, G.; Bakkers, E.; Rivas, J.G. Strong geometrical dependence of the absorption of light in arrays of semiconductor nanowires. *ACS Nano* **2011**, *5*, 2316–2323. [CrossRef] [PubMed]
136. Kempa, T.J.; Tian, B.Z.; Kim, D.R.; Hu, J.S.; Zheng, X.L.; Lieber, C.M. Single and tandem axial p-i-n nanowire photovoltaic devices. *Nano Lett.* **2008**, *8*, 3456–3460. [CrossRef] [PubMed]
137. Mohseni, P.K.; Maunders, C.; Botton, G.A.; LaPierre, R.R. GaP/GaAsP/GaP core-multishell nanowire heterostructures on (111) silicon. *Nanotechnology* **2007**, *18*, 445304. [CrossRef]
138. Yang, Z.-X.; Han, N.; Wang, F.; Cheung, H.-Y.; Shi, X.; Yip, S.; Hung, T.; Lee, M.H.; Wong, C.-Y.; Ho, J.C. Carbon doping of InSb nanowires for high-performance p-channel field-effect-transistors. *Nanoscale* **2013**, *5*, 9671–9676. [CrossRef] [PubMed]
139. Del Alamo, J.A. Nanometre-scale electronics with III-V compound semiconductors. *Nature* **2011**, *479*, 317–323. [CrossRef] [PubMed]

140. Ghahfarokhi, O.M.; Anttu, N.; Samuelson, L.; Aberg, I. Performance of GaAs nanowire array solar cells for varying incidence angles. *IEEE J. Photovolt.* **2016**, *6*, 1502–1508. [CrossRef]
141. Chao, J.-J.; Shiu, S.-C.; Lin, C.-F. GaAs nanowire/poly(3,4-ethylenedioxythiophene): Poly(styrenesulfonate) hybrid solar cells with incorporating electron blocking poly(3-hexylthiophene) layer. *Sol. Energy Mater. Sol. C.* **2012**, *105*, 40–45. [CrossRef]
142. Kelzenberg, M.D.; Turner-Evans, D.B.; Putnam, M.C.; Boettcher, S.W.; Briggs, R.M.; Baek, J.Y.; Lewis, N.S.; Atwater, H.A. High-performance Si microwire photovoltaics. *Energy Environ. Sci.* **2011**, *4*, 866–871. [CrossRef]